

# Observations and Particle-based Simulation of Air-entrainment around a Surface Piercing Cylinder

MARINE 2021

Jun Arai<sup>1,\*</sup>, Takayuki Mori<sup>2</sup>

<sup>1</sup> Naval Systems Research Center (NSRC), Acquisition Technology & Logistics Agency (ATLA), Ministry of Defense, 2-2-1, Nakameguro, Meguro-ku, Tokyo, Japan. Email: arai.jun.we@cs.atla.mod.go.jp, web: <https://www.mod.go.jp/atla>

<sup>2</sup> Naval Systems Research Center (NSRC), Acquisition Technology & Logistics Agency (ATLA), Ministry of Defense, 2-2-1, Nakameguro, Meguro-ku, Tokyo, Japan. Email: mori.takayuki.do@cs.atla.mod.go.jp

\* Corresponding author: Jun Arai, arai.jun.we@cs.atla.mod.go.jp

## ABSTRACT

Flow and air-entrainment around a surface piercing circular cylinder has been investigated experimentally and numerically. In water tunnel experiments, high speed video observations were made for surface piercing flow around a circular cylinder of 150 mm in diameter. Surface pressure measurements were also carried out at nine points around the cylinder. Flow velocity was from 1.5 to 3.0 m/s. The high-speed video observations showed that a pair of air pocket was formed on the side of the cylinder, and bubbles entrained into the air-pockets are shed downstream. The depth of the air-pocket fluctuated in a frequency range lower than the typical Karman vortex frequency. For numerical study, unsteady motion of air-entrainment process was simulated by an MPS method with some corrections to pressure calculation. The MPS calculation reproduced the dynamics of the air-pockets on the side of the cylinder. The time-variation of the predicted air-pocked depth also showed low-frequency fluctuations as observed in the experiment.

**Keywords:** Surface piercing flow; Free-surface interaction; Air-entrainment; Particle method; Recirculating water tunnel; Numerical simulation.

## NOMENCLATURE

$C_{dissp}$	Model constant of a fitting curve for bow wave height [-]
$C_p$	Pressure coefficient [-]
$D$	Cylinder diameter [m]
$Fr$	Froude number [-]
$g$	Gravity acceleration [ $m\ s^{-2}$ ]
$L$	Cylinder vertical length [m]
$L_a$	Air-pocket depth [m]
$L_w$	Submerged length [m]
$p$	Pressure [Pa]
$p_0$	Reference pressure [Pa]
$Re$	Reynolds number [-]
$St$	Strouhal number [-]
$t$	Physical time [s]
$\Delta t$	Time step size for numerical simulation [s]
$U$	Flow velocity [ $m\ s^{-1}$ ]
$\theta$	Angle of position from stagnation point [degree]
$\rho$	Fluid density [ $kg\ m^{-3}$ ]

MPS	Moving Particle Simulation
PND	Particle Number Density
PSD	Power Spectral Density
SPH	Smoothed Particle Hydrodynamics

## 1. INTRODUCTION

Wave and current forces acting on surface piercing objects have been widely studied in the field of offshore structures (Chaplin and Teigen 2003; Noorzaei *et al.* 2005). However most studies have been carried out at relatively low Froude numbers. Flow around a surface piercing cylinder at high Froude number exhibits highly complex features due to large deformation of free-surface accompanied with air-entrainment. Its complexity makes it difficult to understand the detail of phenomena experimentally or numerically.

Recently, Colagrossi *et al.* (2015) reported a numerical simulation and corresponding towing tank test on the surface piercing flow around a submarine mast at relatively high speed up to 6 m/s. They deployed SPH (Smoothed Particle Hydrodynamics) method which was a kind of Lagrangian particle methods and examined improved mast shape to reduce water splashes above the mast. In their SPH simulations, air phase was not taken into account and they pointed out the difficulty of resolving the air-water mixture and droplets by numerical codes. Ageorges *et al.* (2019) reported an observation on the air-entrainment process in the flow around cylinders with diameters from 14 mm to 160 mm. They categorized the entrainment process into two modes, one was a cavity along the cylinder wall and the other was the wake of cylinder. However, their experimental conditions are limited to relatively low Froude numbers up to 1.2 for the larger cylinder diameter, then the flow is not violent and the bubble generation is also moderate.

In spite of the efforts of these recent studies, observations and knowledge about the detailed entrainment process have been restricted in limited range of Reynolds number and Froude number. In this study, surface piercing flow around a cylinder with diameter of 150 mm has been observed with a high speed camera at flow speed  $U$  of 1.5, 2.0, 2.5 and 3.0 m/s in a recirculating water tunnel. Corresponding Reynolds numbers and Froude numbers are from  $Re = 2.3 \times 10^5$  to  $4.5 \times 10^5$  and from  $Fr = 1.2$  to 2.5 respectively. The Reynolds number for the highest speed case is higher than the critical Reynolds number for single phase flow. The high-speed video observation showed that bow wave separated on the cylinder side and ventilated pockets were formed behind the cylinder. Depth of ventilated pockets was to be proportion to  $Fr^2$  as reported by Chaplin and Teigen (2003). Strong unsteadiness appears at larger  $Re$  cases. Numerical simulations were also conducted with MPS (Moving Particle Simulation) method which was another Lagrangian particle-based method like SPH and the structures of ventilated pockets were compared with experimental results.

## 2. EXPERIMENTAL SETUP

The experiments were carried out in a large recirculating water tunnel, Flow Noise Simulator, at the Naval Systems Research Center. The length, width and height of the test section are 10 m, 2.0 m and 2.0 m, respectively. A circular cylinder with diameter  $D = 150$  mm and length  $L = 1,250$  mm was fixed at the top of the test section. Nine pressure sensors (Kyowa Electronic Instruments, PS-05KD) were equipped around the cylinder. The vertical position of the pressure sensors was 275 mm from the cylinder bottom edge as shown in Fig. 1.

Tab. 1 shows the experimental conditions.  $U$  and  $L_w$  are flow speed and immersed length, respectively. Froude number  $Fr$  and Reynolds number  $Re$  were calculated from  $U$  and cylinder diameter  $D$ . In this experiment, submerged length  $L_w$  slightly varied due to difficulty of adjusting the water level at the cylinder with operating the recirculating water tunnel. Reynolds numbers and Froude numbers are ranging from  $Re = 2.3 \times 10^5$  to  $4.5 \times 10^5$  and from  $Fr = 1.2$  to 2.5, respectively. The Reynolds number for the highest velocity exceeds the critical Reynolds number for the single phase flow over a circular cylinder.

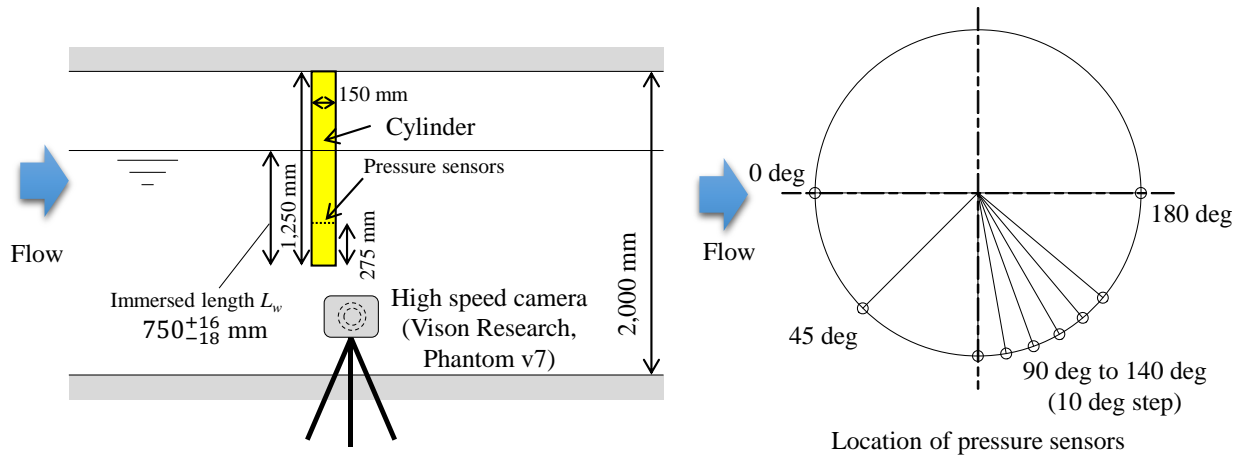


**Figure 1.** Experimental setup.

**Table 1.** Experimental conditions.

$U$ [m/s]	$L_w$ [mm]	Fr	Re
1.5	753	1.2	$2.3 \times 10^5$
2.0	732	1.6	$3.0 \times 10^5$
2.5	766	2.1	$3.8 \times 10^5$
3.0	750	2.5	$4.5 \times 10^5$

### 3. EXPERIMENTAL RESULTS

#### 3.1 Flow Structure and Pressure Distribution

Fig. 2 shows photographs of bow wave for different flow speeds. Bow waves observed by a digital still camera. Height of bow wave is measured manually from these photos. As flow velocity increases, flow becomes unsteady. At  $U \geq 2.5$  m/s, breaking of bow wave was observed. Quantitative analysis will be shown in a later chapter including a comparison with numerical results.

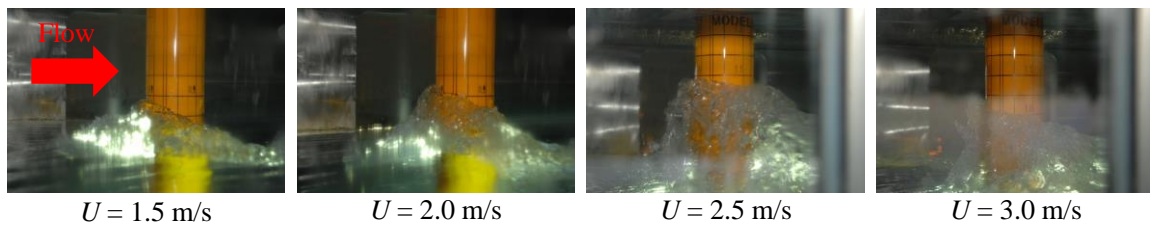


**Figure 2.** Photograph of bow wave.

Fig. 3 shows high-speed video images of entrained bubbles around the cylinder taken from the port side of the cylinder. In all cases, the bow wave separates on the side of the cylinder and air-pockets are formed. Air bubbles are generated in the downstream region. Some bubbles are trapped by vortices and form lined bubbles. Frame ratio is 400 Hz. Red squares show the bottom ends of air-pockets detected by image analysis. The dashed red lines represent the shape of free-surface on the side wall of the water tunnel. As seen from the free-surface shape on the side wall, standing wave is noticeable at  $U = 3.0$  m/s. The height of the standing wave was estimated to be 38 mm by fitting surface shape with a sinusoidal curve. The difference in the water depth

leads to a difference in the cross-sectional area, and results in a variation of the mean velocity. In the present case, the mean velocity was approximately 10 % lower for the largest cross-sectional area than for the smallest one.

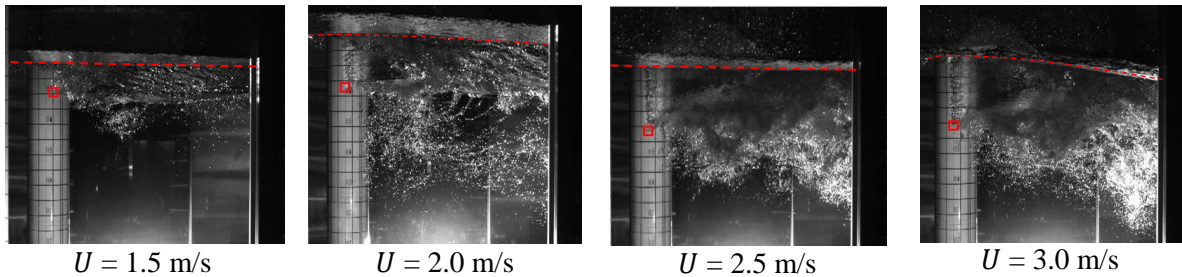


**Figure 3.** Images of air and bubble entrainment for  $U = 1.5 \text{ m/s} \sim 3.0 \text{ m/s}$ .

Mean values of pressure coefficient  $C_p$  around the cylinder surface are shown in Fig. 4. The vertical axis is mean pressure coefficient, which is defined as

$$C_p = \frac{p - p_0}{\frac{1}{2} \rho U^2}, \quad (1)$$

and the horizontal axis is angle of positions of the pressure sensors from the stagnation point of the cylinder. In equation (1), reference pressure  $p_0$  is determined so that  $C_p$  is equal to 1 at  $\theta = 0$  degrees. Pressure almost monotonically decreases and no pressure recovery appears for  $U = 1.5 \text{ m/s}$  and  $2.0 \text{ m/s}$ . On the other hand, pressure recovery is clearly observed for  $U = 2.5 \text{ m/s}$  and  $3.0 \text{ m/s}$  at  $\theta > 90$  degrees. The results indicate that the transition from laminar separation to turbulent separation occurred at around  $2.5 \text{ m/s}$ .

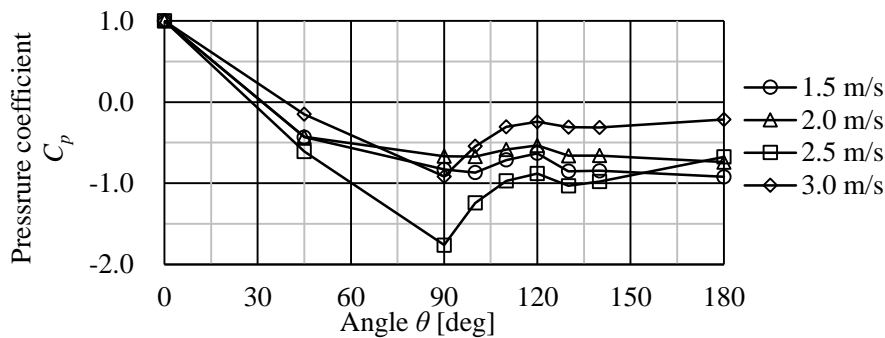


**Figure 4.** Pressure profile around the cylinder.

PSD of pressure coefficient  $C_p$  at  $\theta = 180$  degrees is shown in Fig. 5 for flow speed of  $U = 2.5$  and  $3.0 \text{ m/s}$ . The horizontal axis is Strouhal number calculated from cylinder diameter  $D$  and flow speed  $U$ . Results are average of 39 spectrums calculated using 30,000 data with overlapping 15,000 data of total 600,000 data. There are some peaks around  $St = 0.1$  for both cases. The peak frequency of pressure fluctuation is lower than typical Karman vortex shedding cycle ( $St = 0.2$ ).

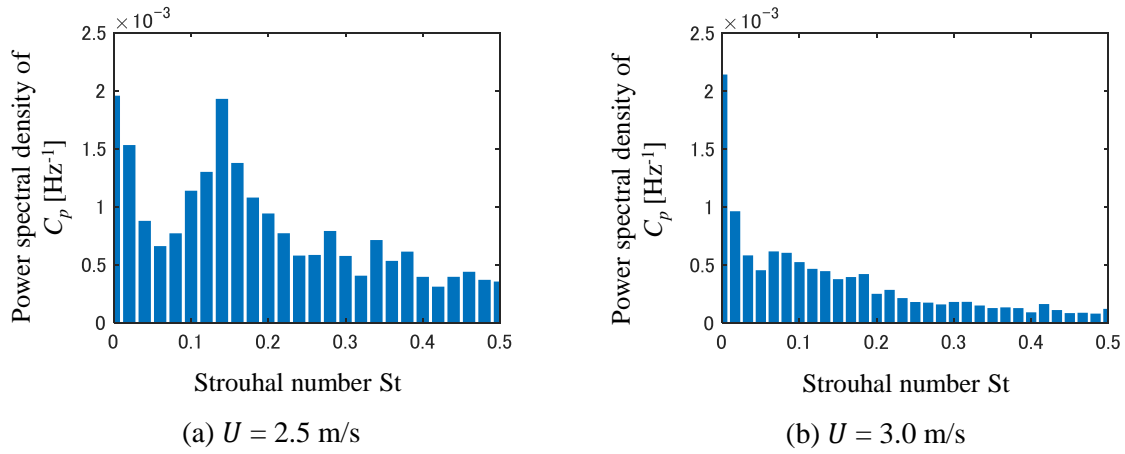


**Figure 5.** Power spectral density of pressure at  $\theta = 180$  degrees.

### 3.2 Air-pocket Depth

As shown in Fig. 3, air-pockets are formed on the side of the cylinder. The depth of these air-pockets  $L_a$  is tracked by analyzing the high-speed video images and shown in Fig. 6. Green, blue, red and black lines show the results for 1.5 m/s, 2.0 m/s, 2.5 m/s and 3.0 m/s, respectively. Error bars for mean value plots are standard deviation. Time histories of  $L_a$  show relatively mild variations at low flow speeds and more oscillatory variations at higher speed cases, 2.5 m/s and 3.0 m/s. Sudden changes of  $L_a/D$  observed from about 3.0 sec to 4.5 sec at 1.5 m/s are measurement artifacts caused by small floating bubbles originating from entrained air behind the cylinder. The mean values of air-pocket depth  $L_a$  are shown in Fig. 6 (b). The empirical equation of Chaplin and Teigen (2003) gives a good estimation for  $L_a/D$ . As mentioned in the previous section, the flow transits from laminar to turbulence separation at around 2.5 m/s. Despite the transition of the flow pattern,  $L_a/D$  still has a correlation with  $Fr^2$  up to 3.0 m/s.

PSDs of air-pocket depth are shown in Fig. 7 for  $U = 2.5$  and 3.0 m/s. The horizontal axis is Strouhal number calculated from cylinder diameter  $D$  and flow speed  $U$ . Results are average of 8 spectrums calculated using 1,000 data with overlapping 750 data for total 3,000 data. Dominant frequency does not appear clearly, however, the power concentrates on  $St < 0.2$  for both cases. These trends are similar to the PSD of pressure fluctuation in Fig. 5.

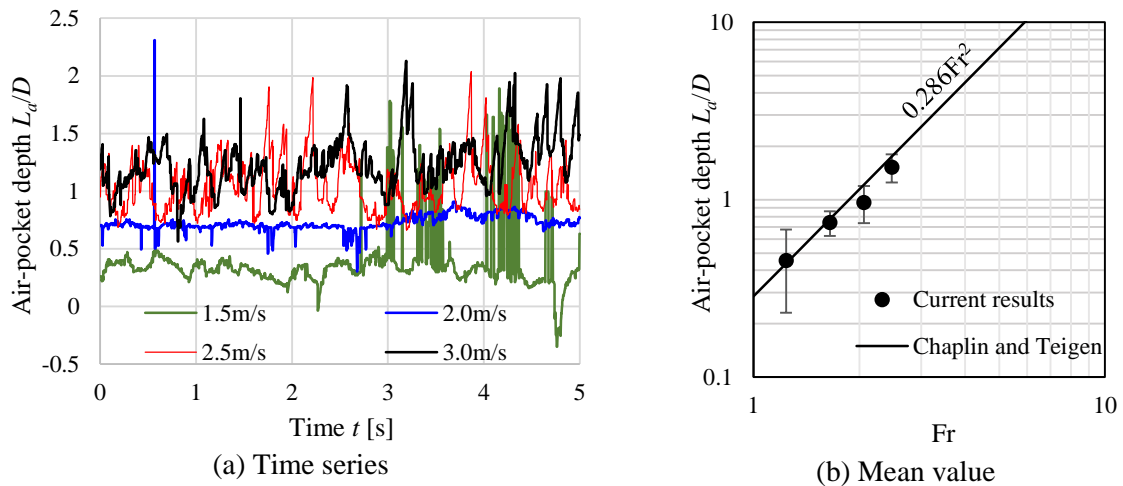


**Figure 6.** Air-pocket depth.

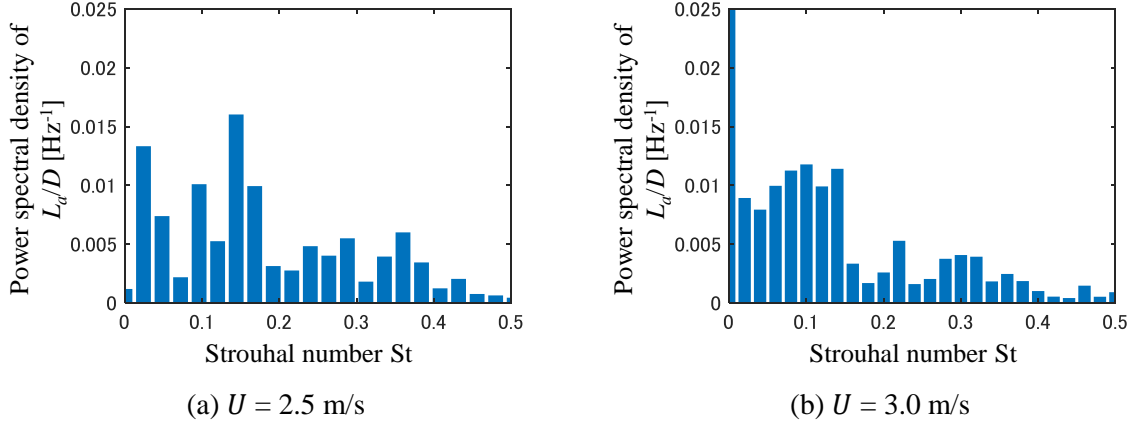


**Figure 7.** Power spectral density of air-pocket depth fluctuation.

## 4. NUMERICAL ANALYSIS

### 4.1 Moving Particle Simulation

An MPS (Moving Particle Simulation) method, originally called a Moving Particle Semi-implicit method, is employed to simulate the surface piercing flow around the cylinder. The MPS method is one of Lagrangian particle-based methods. The detail of the MPS method can be found in Koshizuka and Oka (1996). Some modifications in a pressure equation were added to stabilize calculations against the original MPS method. A polygon wall model (Harada *et al.*, 2008) was used to represent the wall and cylinder surfaces. A surface tension model using inter-particle potential force (Kondo *et al.*, 2007) was also incorporated.

In the original MPS method, the pressure equation is formulated with particle number density (PND) based a source term as follows.

$$\nabla^2 P_i^{k+1} = -\frac{\rho}{n_0 \Delta t} \frac{n_i^* - n_0}{\Delta t} \quad (2)$$

In this paper, the right hand side of equation (2), i.e. source term, is modified by using blends of particle number based source term and velocity divergence based source term. (Tanaka and Masunaga, 2010) PND based source term is also modified as using blends of the base PND and PND of the previous time step.

$$\nabla^2 P_i^{k+1} = \frac{\rho}{\Delta t} \left[ \alpha_{div} \langle \nabla \cdot \vec{u}^* \rangle_i - (1 - \alpha_{div}) \frac{2 n_i^* - \{\beta_n n_0 + (1 - \beta_n) n_i^k\}}{\Delta t n_i^* + \{\beta_n n_0 + (1 - \beta_n) n_i^k\}} \right] \quad (3)$$

Where  $\alpha_{div}$  and  $\beta_n$  are model constants ranging from 0.0 to 1.0 for blend ratios of divergence based source term and the base density  $n_0$ , respectively. Superscripts  $k$  and  $*$  are a number of time step and intermediate step between  $k$  and  $k + 1$ . The subscript  $i$  is an index of an arbitrary particle. Larger  $\alpha_{div}$  and  $\beta_n$  tend to suppress numerical oscillation of pressure, however too large values cause deviation of incompressibility.  $\alpha_{div} = 0.8$  and  $\beta_n = 0.5$  are used in this study.

### 4.2 Numerical Setup

The dimensions of the calculation region are  $6.0 \text{ m} \times 2.0 \text{ m} \times 2.0 \text{ m}$ . The cylinder center is located at  $1.0 \text{ m}$  from an inflow boundary, as shown in Fig. 8. Calculation region represents a part of the test section of Flow Noise Simulator. Three layers of inflow particles are placed for inflow boundary condition. Inflow condition is represented by moving wall particles that will change into fluid particles after moving over particle average distance. For outflow boundary condition, outflow particles are placed outside of the outflow boundary to keep particle number density of fluid particles adjacent to the outflow boundary. Velocity of particles near the

outflow boundary is fixed to same as inflow velocity to keep the water level in the calculation region. Particle size is 12.5 mm and the number of particles is about 6 million. Time step  $\Delta t = 0.5$  msec for  $U = 1.5$  m/s,  $\Delta t = 0.25$  msec for  $U = 2.5$  m/s,  $\Delta t = 0.2$  msec for  $U = 3.0$  m/s. Physical time of 7.5 sec were calculated and results after 2.0 sec were used for analysis in the next section.

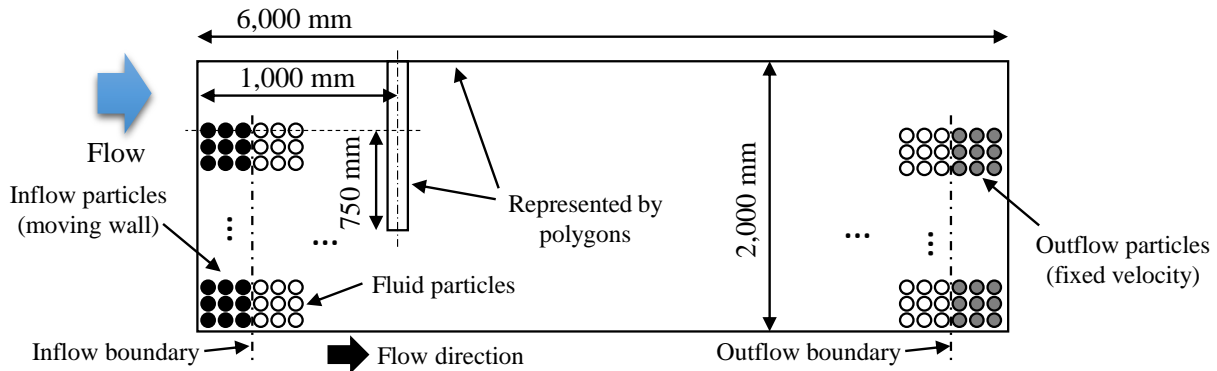


**Figure 8.** Calculation region.

## 5. NUMERICAL RESULTS

Free-surface particles viewed from port side of the cylinder are shown in Fig. 9. Fig. 9 shows visualization of MPS calculations for  $U = 1.5$  m/s, 2.5 m/s and 3.0 m/s at 4.5 sec. Blue particles represent free-surface particles. Red squares show bottom ends of air-pockets which correspond to those in Fig. 3. Bow wave separates on the side of the cylinder and air-pockets are formed. These observations are similar to the high-speed camera measurements shown in Fig. 3. In the current MPS calculation air phase is neglected and also small air bubbles cannot be resolved due to insufficient particle size, however it can be considered that free surface particles represent entrained air in the adjacent region of the cylinder because it takes some time for free surface particles to collapse. Behind the cylinder, troughs of entrained air are characteristically observed at certain intervals for higher two cases. It appears that the troughs of entrained air are relative to vortex shedding behind the cylinder. Notably, depth of these troughs is a few times deeper than air-pocket depth. Air bubbles originating from deeply entrained air will travel to downstream without reaching to water surface and result in bubble wake. Therefore, predicting not only air-pocket depth but also depth of air entrainment is important. These troughs are not clearly visible in Figure 3, however there seems to be low and high bubble density regions also in high speed images by observing carefully. Above results indicate that the MPS method has a possibility of handling these complex phenomena, although further quantitative validation will be required.

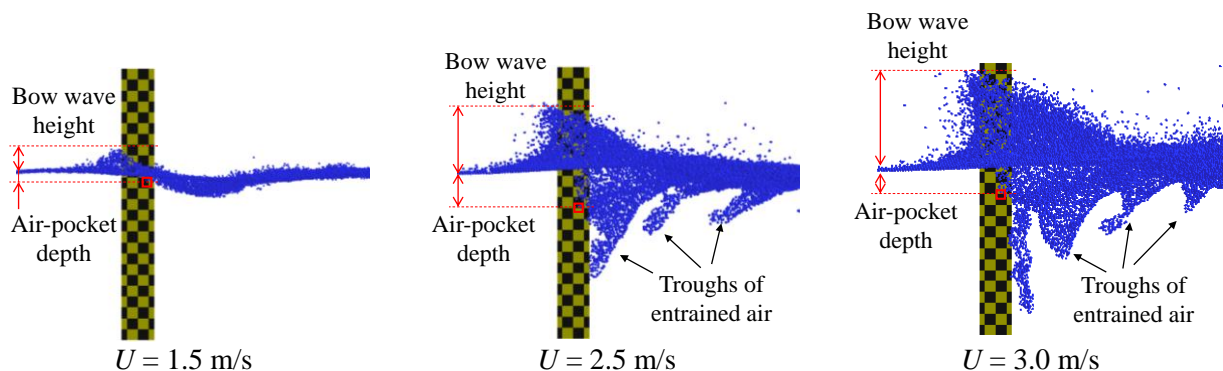


**Figure 9.** Side view of calculation results at 4.5 sec.

Fig. 10 shows mean bow wave height obtained from experimental photographs and MPS simulations as a function of  $Fr^2$ . The white circles and squares are experimental and numerical results, respectively. These are averages of five photographs or 551 results of MPS calculation from 2.0 sec to 7.5 sec. The black and red lines are a theoretical estimation calculated from Bernoulli's equation and an empirical equation suggested by

Keough *et al.* (2016) which has dissipation term proportional to square of flow speed against Bernoulli's equation. Where  $g$  is gravity acceleration and  $C_{dissp}$  is a constant with a value of 0.005. Both lines give good estimation for current experimental results except for  $Fr^2 = 6.1$  ( $U = 3.0$  m/s). The reason for this discrepancy is unclear, but it is possible that the effect of standing wave in the water tunnel becomes larger at higher flow speed and is not negligible. On the other hand, MPS results show a good correlation with Keough's equation including  $Fr^2 = 6.1$ .

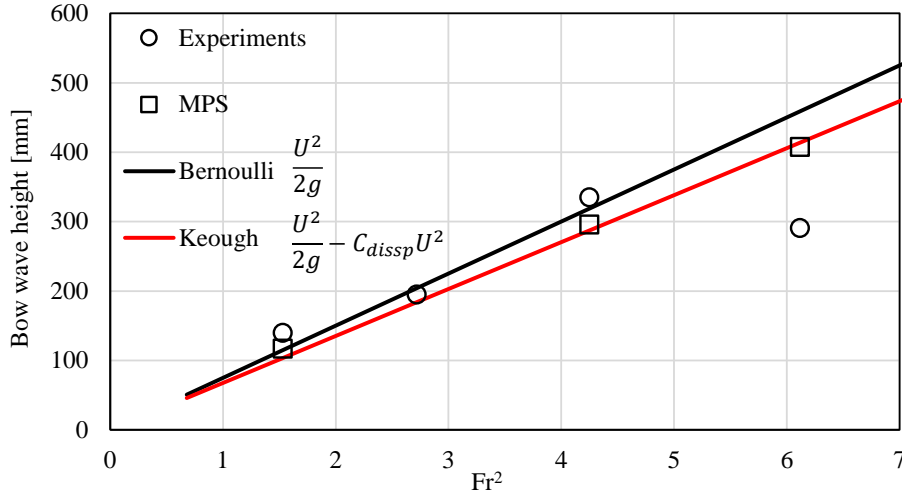


**Figure 10.** Bow wave height as a function of Froude number squared.

Pressure distribution is shown in Fig. 11. Pressure coefficient  $C_p$  is defined as same as equation (1). In the MPS result, pressure recovery can be found at 2.5 and 3.0 m/s at  $\theta > 90$  degrees, while no clear recovery appears at 1.5 m/s as same as experimental results. However, the MPS results tend to underestimate pressure drop at the side of the cylinder and overestimate recovered pressure for higher two cases. On the other hand, pressure at 180 degrees shows a good agreement between the MPS result and the experimental result except for 3.0 m/s. As mentioned in section 3.1, the experimental result of 3.0 m/s might be influenced by standing wave in the water tunnel. Another reason of this underestimation could be due to the limitation of minimum pressure in MPS calculation. To stabilize pressure calculation negative pressure is forced to be corrected into free-surface pressure which is usually set to zero.

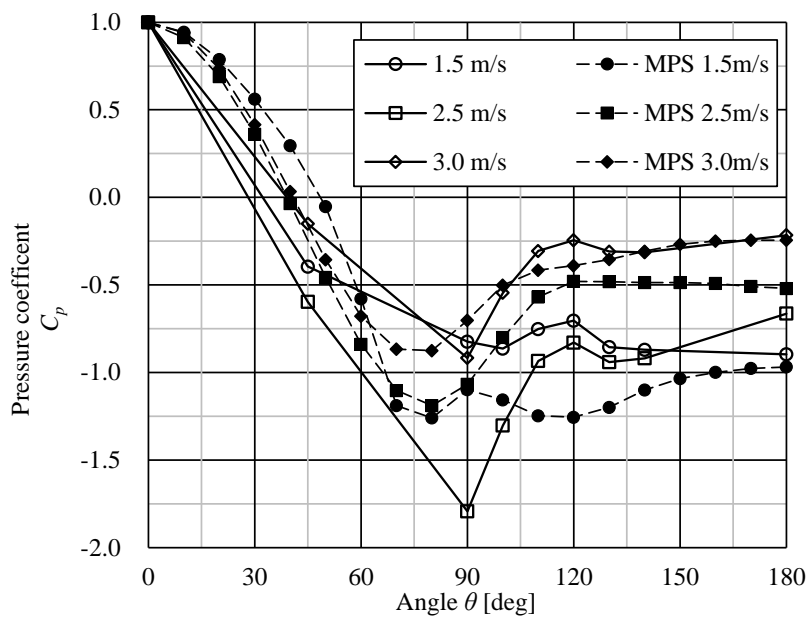


**Figure 11.** Pressure distribution of MPS and experimental results.

Time series and mean value of air-pocket depth  $L_a/D$  are shown in Fig. 12. Green, red and black lines show the results for 1.5 m/s, 2.5 m/s and 3.0 m/s, respectively. Error bars for mean value plots are standard deviation. As same as the experimental results, time histories of  $L_a$  seem to be moderate at low flow speed and more oscillatory at higher speed cases. With regard to mean values, MPS results underestimate the Chaplin and Teigen line and results of 2.5 m/s and 3.0 m/s are reversed. As mentioned above, restricting negative pressure could be one of the reasons of this underestimation. Further studies will be required including the influence of Reynolds number as mentioned in 3.2.

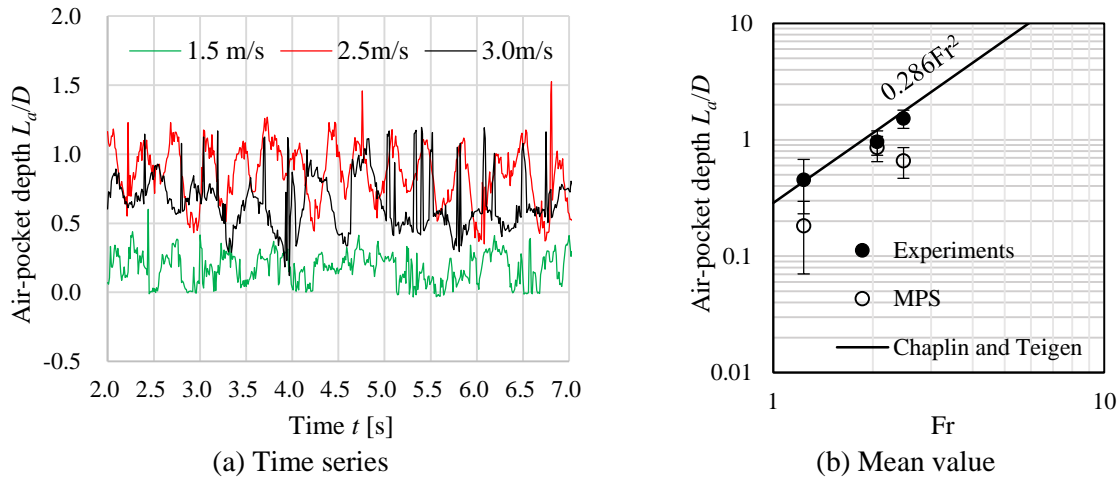


**Figure 12.** Air-pocket depth of MPS results.

PSD of air-pocket depth is shown in Fig. 13 for flow speed  $U$  of 2.5 and 3.0 m/s. The horizontal axis is Strouhal number calculated from the cylinder Diameter  $D$  and flow speed  $U$ . Results are average of 7 spectrums calculated using 250 data with overlapping 200 data for total 750 data. Dominant frequencies are clearly appeared against with experimental results. Underestimation of turbulence diffusion due to insufficient resolution might cause these clear peaks. Nevertheless, the peaks are around  $St = 0.1$  which is lower than usual cycle of Karman vortex shedding and this trend is same as experimental results in Fig. 7.

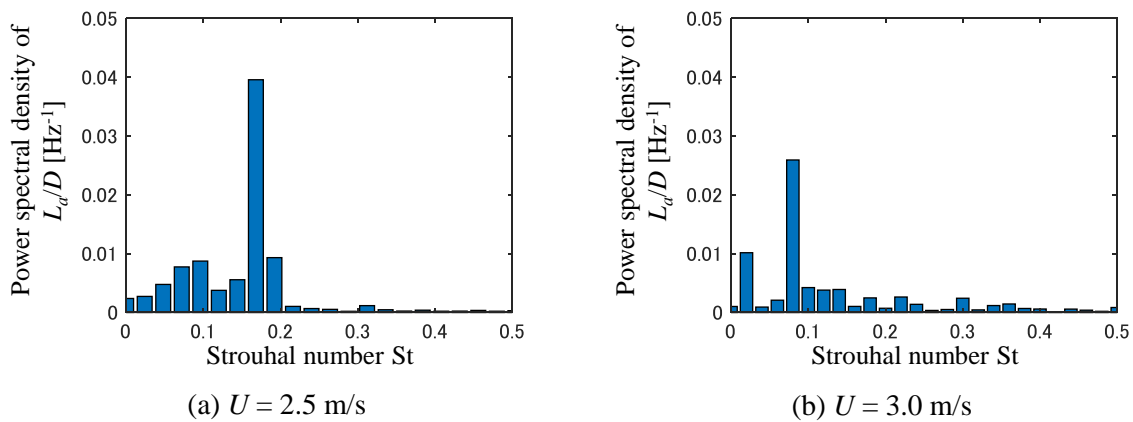


**Figure 13.** Power spectral density of air-pocket depth fluctuation of MPS results.

## 6. CONCLUSIONS

Structures of air-entrainment around a surface piercing cylinder has been observed in a recirculating water tunnel and numerically investigated by a Lagrangian particle method. The cylinder diameter was 150 mm and flow velocity ranged from 1.5 to 3.0 m/s. In this study, the structure of air-pocket has been extensively surveyed not only statistically but also in time domain. As a result, the power of air-pocket depth fluctuation concentrated on the lower frequency than the typical frequency of Karman vortex shedding.

An MPS method with some corrections to pressure calculation has successfully simulated unsteady motion of air-entrainment process of the flow around the surface-piercing cylinder. Although the MPS result overestimated pressure drop and its recovery, the overall tendency appeared to be same as experimental results in terms of the formation of air-pocket on the side of the cylinder. The dominant frequency of air-pocket depth fluctuation was lower than the usual Karman vortex shedding cycle.

## REFERENCES

- Ageorges, V., Peixinho, J. and Perret, G. (2019). Flow and Air-entrainment around Partially Submerged Vertical Cylinders. *Phys. Rev. Fluids*, 4, 064801.
- Chaplin, J. R. and Teigen, P. (2003). Steady Flow Past a Vertical Surface-piercing Circular Cylinder. *J. Fluids Struct.*, 18(3-4), 271-285.
- Colagrossi, A., Marrone, S., Bouscasse, B. and Broglia, R. (2015). Numerical Simulations of the Flow Past Surface-piercing Objects. *Int. J. Offshore Polar Eng.*, 25(01), 13-18.
- Harada, T., Koshizuka, S. and Shimazaki, K. (2008). Improvement of Wall Boundary Calculation Model for MPS Method. *Transactions of JSCEs*, 20080006. (in Japanese)
- Keough, S. J., Kermonde, I. L., Amiet, A., Phillip, J., Ooi, A., Monty, J. P. and Anderson, B. (2016). Time Resolved Measurements of Wake Characteristics from Vertical Surface-Piercing Circular Cylinders. *20th Australasian Fluid Mechanics Conference*, dates, Perth, WA, Australia.
- Kondo, M., Koshizuka, S. and Takimoto, M. (2007). Surface Tension Model using Inter-particle Potential Force in Moving Particle Semi-implicit Method. *Transactions of JSCEs*, 20070021. (in Japanese)
- Koshizuka, S. and Oka, Y. (1996). Moving-Particle Semi-Implicit Method for Fragmentation of Incompressible Fluid. *Nuclear Science and Engineering*, 123, 421-434.
- Noorzaei, J., Bahrom, S. I., Jaafar, M. S., Thanoon, W. A. M. and Mohammad, S. (2005). Simulation of Wave and Current Forces on Template Offshore Structures. *Suranaree J. Sci. Technol.*, 20(3), 193-210.
- Tanaka, M. and Masunaga, T. (2010). Stabilization and Smoothing of Pressure in MPS Method by Quasi-Compressibility. *Journal of Computational Physics*, 229(11), 4279-4290.